# All-Carbon Hybrid Mobile Ion Capacitors Enabled by 3D Laser Scribed Graphene

Fan Zhang[a], Wenli Zhang[a], Jing Guo[a], Yongjiu Lei[a], Mushtaq A. Dar[b], Zeyad Almutairi[c,d], Husam N. Alshareef [a,*]

[a]Materials Science and Engineering, Physical Science & Engineering Division, King Abdullah University of Science and Technology (KAUST), Thuwal, 23955-6900, Saudi Arabia

[b]Center of Excellence for Research in Engineering Materials, College of Engineering, King Saud University, Riyadh, 11421, the Kingdom of Saudi Arabia

[c]Mechanical Engineering Department and [d]Sustainable Energy Techonologies Cetner, College of Engineering, King Saud University, Riyadh 11421, Saudi Arabia

E-mail: *husam.alshareef@kaust.edu.sa*

**KEYWORDS:** Laser scribed, Nitrogen-doped, Graphene, Hybrid mobile ion capacitors, High energy density.

## ABSTRACT

Hybrid mobile ion capacitors (HMIC) have been proposed as a way to incorporate the advantages of both batteries and supercapacitors into one system. Unfortunately, considering the much slower $Li^+$ intercalation/deintercalation process, finding a suitable battery anode material with high rate performance is still a major challenge. Here, we report the fabrication of laser scribed nitrogen-doped graphene (NLSG) with 3D structure as binder-free, and conductive additive-free anode. This NLSG anode has high nitrogen and oxygen doping (8.6 at% and 6.3 at%) leading to the formation of conductive electrodes with expanded lattice spacing, providing more convenient pathways and reaction sites for $Li^+$ ions. Hybrid Li-ion capacitors (HLIC) were assembled by combining the NLSG anodes with hierarchical porous carbon (PC) cathodes

This article has been accepted for publication and undergone full peer review but has not been through the copyediting, typesetting, pagination and proofreading process, which may lead to differences between this version and the Version of Record. Please cite this article as doi: 10.1002/ente.202000193

obtained by pyrolysis of Ethylenediaminetetraacetic (EDTA) tetrasodium salt. The NLSG//PC hybrid Li-ion capacitors show an energy density (including the total weight of two electrodes) of 186 Wh $kg^{-1}$ at 200 W $kg^{-1}$. Even when power density increased to the level of conventional supercapacitors (20 kW $kg^{-1}$), an energy density of 76 Wh $kg^{-1}$ can still be obtained. Further, the devices exhibit excellent cycle life, retaining 87.5% of the initial value after 5000 cycles. This study demonstrates that laser scribed graphene is a very promising electrode for mobile ion capacitors.

## INTRODUCTION

Among various electrochemical energy storage systems, batteries and supercapacitors are currently recognized as one of the most promising devices. Lithium and sodium ion batteries possess relatively high energy density (100–200 Wh $kg^{-1}$) but suffer from low power density and poor cycle life.[1] The supercapacitors exhibit outstanding power density (as high as 10 kW $kg^{-1}$) and cycle life; however, their low energy density limits their useful application.[2] Given these issues, developing hybrid energy storage systems that integrate the advantages of both batteries and supercapacitors is a viable solution.

Hybrid mobile ion capacitors (HMIC) are one type of hybrid supercapacitors, which were proposed in the early 2000s.[3] They are assembled using a battery-type anode to provide high energy density, and a capacitor-type cathode to provide high power density. During the charge and discharge process, anion adsorption/desorption occurs on the surface of the cathode, whereas lithium ion intercalation/deintercalation occurs within the anode.[4] One of the key limitations in developing high-performance HMICs is the imbalance in the power capability of the two electrodes. Several electrode materials have been proposed for hybrid Li-ion capacitors (HLIC) such as B-Si/$SiO_2$, $TiP_2O_7$, $Fe_3O_4$/3D graphene, and $V_2O_5$.[5] Unfortunately, most of those

materials suffer from either high-cost or tedious processes, thus hindering their use.[6] Currently, the most widely used cathode material in HMICs is activated carbon due to its favorable mertis that inlcude chemical stability, low cost, and tunable HMIC structure. In general, the anode insertion kinetics of $Li^+$ is much slower than the cathode physical adsorption/desorption. Therefore, the selection of the anode material with good rate performance is still a major challenge in HLICs.[7]

Laser scribed graphene (LSG) is a porous polycrystalline graphene film with 3D networks, which was initially derived from commercial polymer films. LSG film has exhibited promising performance in various applications, including electrochemical sensors, supercapacitors, biosensors, and hydrogen evolution reactions.[8] Furthermore, it has been demonstrated that nitrogen doping can significantly enhance the surface area, enlarge the carbon interlayer distance, increase the active sites, and improve the electrode kinetics of the carbon materials. Recently, our group has developed nitrogen-doped laser scribed graphene (NLSG) directly bonded to the current collectors. As we know, compared with Li ions, sodium ions are much harder to be intercalated/deintercalated in carbon lattices due to the larger atomic radius. However, our conductive and additive-free NLSG film exhibited excellent performance as a sodium-ion battery anode. A capacity of 425 mAh $g^{-1}$ at 0.1 A $g^{-1}$ and a capacity of 148 mAh $g^{-1}$ at a high current density of 10 A $g^{-1}$ were obtained with excellent cycling stability. Thus we decided to evaluate our NLSG films as anodes for HLIC.[9]

## RESULTS AND DISCUSSION

Figure 1a shows a schematic illustrating the laser-scribing process of nitrogen-doped graphene. Firstly, urea was used as a nitrogen source and dissolved into the polyamic acid (PAA)

solution by stirring. The solution was then casted onto Cu foil with a scraper. The PAA/urea film was dried followed by exposing to $CO_2$ laser irradiation with $N_2$ gas flow. Since the laser source can provide high local temperatures up to 1000 °C, the film will is transformed into 3D porous graphene with the simultaneous decomposition of urea into nitrogen and incorporation of nitrogen into the graphene lattice.[10] The final product is henceforth referred to as nitrogen-doped laser-scribed graphene (NLSG). More details about this process can be found in the Experimental Section.

Figure 2a shows the X-Ray Diffraction (XRD) pattern of NLSG. Two broad peaks at 24.1° and 42.5° are observed, which can be attributed to (002) and (100) reflections of crystallized carbon, respectively. The characteristic peak of the (002) planes corresponding to the d-spacing values of 0.375 nm, which is much higher than conventional graphite (d-spacing ~ 0.336 nm), indicating that interlayer spacing is enlarged with nitrogen doping and laser treatment. Theoretical calculations and experimental work have shown that the expanded interlayer distance allows higher levels of reversible Li and Na intercalation into the carbon materials.[11] Besides, the broad and asymmetric nature of the (002) peak demonstrates some degree of disordered structure in the NLSG sample. The crystallite size of NLSG can be calculated based on the well-known Scherrer equation, $L_{(hkl)} = K\lambda / \beta \cos\theta$, using the full width at half maximum value of the (002) and (100) peaks. The values along the c-axis (Lc) and a-axis (La) are calculated to be 3.5 nm and 11.5 nm. Therefore, we can estimate that our resultant NLSG anodes are composed of 8-10 (e.g., 3.5/0.375=9.3) graphene sheets.[12]

The Raman spectra is a fast and reliable technique for characterizing the degree of order in carbonaceous materials. Figure 2b presents the Raman spectra of our NLSG anodes. As we can see, three picks located at 1350, 1600, and 2650 $cm^{-1}$ can be detected, which are typical for

D, G, and 2D bands of graphitic materials. The D band can be assigned to disordered carbon or defective graphitic structures, the G band can be assigned to graphitic in-plane vibrations, while the 2D band can be assigned to the second-order zone-boundary phonons. The intensity ratio between G band and D band is indicative of the degree of graphitic ordering in the NLSG.[13] The value of $I_D/I_G$ for NLSG is calculated to be 1.35, indicating abundant defects and structural distortion in the NLSG sample. The 2D band is sensitive to the stacking order of the polyaromatic layers due to strong interlayer interactions. The shape of the 2D band is a single broad peak, which suggests that the graphene produced by the laser-scribing process is a turbostratic stack, with full width at half maximum (FWHM) of be 72 $cm^{-1}$.[14]

The thermal decomposition characteristics of pure NLSG powder was investigated using thermogravimetric analysis (TGA), which was conducted from room temperature to 1000 °C at a heating rate of 10 °C $min^{-1}$. As shown in Figure 2c, the minor weight loss of the NLSG sample from 25 to 150 °C can be ascribed to the evaporation of unstable water. After that, the removal of residual oxygenated functional groups will occur within a temperature range of 150 °C to 470 °C.[15] Since our sample contains some amount of nitrogen and oxygen atoms (will be discussed later), the weight loss will continue up to 1000 °C and the total weight loss is around 15%.

X-ray photoelectron spectroscopy (XPS) measurement was performed to confirm the incorporation of heteroatoms and the level of nitrogen doping in our NLSG sample. Figure S1a displays the high-resolution C 1s spectra. Noticeable broadened signals can be detected on the high energy side (286–290 eV), indicating the presence of carbon atoms singly or doubly coordinated with oxygen and nitrogen atoms. By fitting the spectra, three peaks can be found, corresponding to carbon atoms existing in different functional groups: $sp^2$ carbon (at 284.5 eV),

the combination of $sp^3$ carbon and C−N bonding (at 285.5 eV), and N−C=O bonding (at 289.0 eV).[16] This observation further confirms the successful transformation of the PI film into a graphitic form of carbon and the simultaneous nitrogen bonding into the graphene framework. The nitrogen functionalities are mainly represented by peaks at 398.1, 400.0 and 401.4 eV (Figure S1b), and these are assigned to pyridinic, pyrrolic and graphitic nitrogen, respectively. Our NLSG sample contains a high level of 8.6 at% nitrogen and 6.3 at% oxygen. It has been demonstrated that nitrogen-containing groups are beneficial to the conductivity, while oxygen can play a positive role for Li storage by increasing disorders, defects, and local electron density around O atoms.[17]

The $N_2$ adsorption isotherms of NLSG is shown in Figure S2a. The NLSG sample shows a typical type-Ⅱ isotherms curve. The total Brunauer−Emmett−Teller (BET) specific surface areas of NLSG is calculated to be 456 $m^2\ g^{-1}$. Figure S2b shows the pore size distributions, obtained by the Density Functional Theory (DFT) method from the desorption branch of the isotherm. The NLSG sample mainly contains micropores (<2 nm) and mesopores (2–10 nm).[18] The laser-scribing process can provide high local temperature, which leads to the rapid liberation of gaseous products and the formation of 3D structure. The simultaneous heteroatom doping can expand the carbon lattice and create disorders, resulting in NLSG with high surface area and high porosity.

The morphology and microstructure of the NLSG samples were further investigated by scanning electron microscopy (SEM) and transmission electron microscopy (TEM). As shown in Figures 2d and 2e, NLSG displays a highly corrugated 3D graphene architecture. The graphene sheets are ultrathin, and the thickness is uniform (Figure 2f). It's worth mentioning that our NLSG electrode adheres tightly with the Cu foil without binder. The top and side view SEM

images of NLSG electrodes from are shown in Figure S3a and S3b, respectively. It can be seen that all the PI precursor has been transformed to NLSG sheet, and the thickness of NLSG sheet is around 30 μm. Figure 2g reveals one wrinkled NLSG nanosheet, the lateral size of which is about 5 μm. Under close observation from high-resolution TEM (HRTEM) image in Figure 2h, ultrathin graphene sheets of 4-5 nm are interconnected with numerous micropores in between, we can deduce that the interlayer spacing in this sheet is 0.38 nm, agreeing well with the XRD results. Figure 2i shows one typical NLSG nanosheet and corresponding elemental maps. It can be seen that C, N and O atoms are uniformly distributed throughout the nanosheet. To acquire more accurate data about the thickness of NLSG nanosheets, atomic force microscopy (AFM) analysis was performed. As shown in Figure S4, the NLSG nanosheets have a flat surface, with thickness of around 4 nm and lateral sizes of around 2-5 μm, which matches very well with the XRD and TEM data.

The porous carbon (PC) cathode was obtained by pyrolysis of EDTA tetrasodium salt, more details about this process can be found in the Figure 1b and Experimental Section. The XRD pattern of PC (Figure S5a) shows two broad peaks at 25° and 43°, which were attributed to the (002) plane and (001) plane reflection, respectively, and this reveals the presence of amorphous carbon.[11] The Raman spectra (Figure S5b) of our PC sample shows two picks. The first one is located at 1354 $cm^{-1}$, which corresponds to the breathing mode vibration of $A_{1g}$, associated to disordered carbon. Another peak at 1591 $cm^{-1}$ relates to the in-plane stretching vibration mode of $E_{2g}$ in $sp^2$ hybridized carbons.[13] SEM and TEM images of PC are shown in Figure S5c-S5e. Macropores in the range of 50-100 nm can be detected, with 3D linked carbon skeleton which results on higher specific surface area. The disordered structure of PC can be detected in HRTEM shown in Figure S5f. The $N_2$ adsorption isotherms of PC are shown in

Figure S6a, showing a BET specific surface area of 1886 $m^2 g^{-1}$. Figure S6b shows the pore size distributions calculated by the DFT method, showing that the PC sample contained a significant concentration of micropores (<2 nm). To sum up, the obtained PC sample possessed hierarchical micro-and macro-pores, a high specific surface area of 1886 $m^2 g^{-1}$ and 3D architecture. This unique 3D structure generated abundant interconnected pore structure that allowed the electrolyte to be stored therein, reducing the distance that the electrolyte travels on the surface of the electrode material. At the same time, abundant micropores and mesopores exist on the surface of carbon materials. This type of pore structure results in high energy density.

Our NLSG sample was used as anode material for hybird Li-ion capacitors, while PC was used as cathode material. Before we check the performance of the HLICs, half-cell tests were carried out on NLSG and PC using coin cells with Li foil used as both counter and reference electrodes. For the lithium half-cell performance, typical cyclic voltammetry (CV) curve of NLSG anode were tested between 0.01 and 2.5V (vs Li/Li+) at a scan rate of 0.1 mV $s^{-1}$, as shown in Figure 3a. The first CV scan displayed one irreversible reductive peak at about 0.7 V, which can be ascribed to the electrolyte decomposition and the formation of a solid electrolyte interphase (SEI).[19] This peak disappeared during the subsequent cycles, suggesting stable SEI formation in the initial cycle. A pair of broad redox peaks below 0.5 V during lithiation and 0-0.7 V during delithiation were observed, indicating the insertion/extraction of lithium ions into the defective graphene interlayers.[20] After the first cycle, the voltammograms became overlapped, indicating excellent reversibility of the NLSG anode. Figure 3d shows the CV curves of PC cathode tested between 2.5 and 4.0 V (vs Li/Li+) at a scan rate of 0.1 mV $s^{-1}$. It's worth mentioning here that the cathode we used is free-standing PC film with PTFE as binder and carbon black as additive, for which the preparation process can be found in Figure S7. The CV

curves for PC exhibit good rectangular shapes with small humps, indicating that the dominant electrochemical charge storage is double-layer capacitance, which can be ascribed to the anion ($PF_6^-$) adsorption/desorption. The pseudocapacitance contribution is smaller and can be attributed to the interaction between the electrolyte and active carbon surface.[21]

The galvanostatic charge/discharge curves of NLSG and PC were measured at a current density of 0.1 A $g^{-1}$ in the voltage range of 0.01–2.50 V and 2.5-4.0 V (vs Li/Li+), respectively, as shown in Figure 3b and 3e. For NLSG anode material, the first discharge curve presents a flat plateau at around 0.7 V due to the SEI formation, and the sloping profile below 0.5 V, which correspond to the lithium intercalation process.[9] The NLSG anode exhibits an initial discharge capacity of 905 mAh $g^{-1}$ and charge capacity of 624 mAh g-$^{1}$ at 0.1 A $g^{-1}$, with an initial coulombic efficiency (CE) of 68%. After the first cycle, CEs of NLSG rapidly increased to 99.5% and remained stable. After 50 cycles, the NLSG anode exhibits a high reversible capacity of 568 mAh $g^{-1}$. For PC cathode material, linear charge-discharge curves can be observed, indicating ideal capacitive behavior. After 50 cycles, PC cathode exhibits a reversible capacity of 55 mAh $g^{-1}$.

Both of NLSG and PC electrodes have a good rate and cycling performance. Even at a high current density of 10 A $g^{-1}$, NLSG can deliver a specific capacity of 212 mAh $g^{-1}$, while PC can deliver 23 mAh $g^{-1}$, as shown in Figure 3c and 3f. When the current density is reduced to 0.1 A $g^{-1}$, NLSG and PC electrodes exhibit excellent capacity retention. Furthermore, NLSG and PC were galvanostatically discharged and charged at 0.1 A $g^{-1}$ during the first 20 cycles for activation and then at 10 A $g^{-1}$ for the following 1000 cycles. As shown in Figure S8, after 1000 cycles, NLSG maintains 88% of the initial capacity, while PC maintains 95% of initial capacity, indicating superior high rate cycling stability.

The HLIC devices were assembled using NLSG as the anode and PC as the cathode. To obtain an extended potential window and avoid overcharging, NLSG anode was pre-lithiated and fixed at 0.05 V vs. $Li/Li^+$.[22] To balance the charge between NLSG and PC, the optimized mass ratio of cathode to anode was determined to be about 1: 3 (as shown in Figure S12). By using NLSG anode and PC cathode, a full hybrid mobile ion capacitor was constructed using 1 m $LiPF_6$ electrolyte. During charge and discharge, $PF_6^{-1}$ ions are adsorbed/desorbed on the surface of PC, whereas Li ions are intercalated/deintercalated within NLSG, as schematically illustrated in Figure 1c.

Figure 4a displays the CV curves of NLSG//PC hybrid Li-ion capacitor at the scan rate of 1 mV $s^{-1}$. In the first anodic scan, three peaks at 1.5, 2.3 and 3.5 V can be detected. While in the first cathodic scan, three peaks at 3.7, 3.3 and 2.3 V can be found. After 2 cycles, the CV curves become smoother, with only four obvious and reversible peaks at 2.5 and 3.5 V (anodic scan), 3.3 and 2.3 V (cathodic scan) remaining. These pairs of redox peaks are related to the intercalation and surface redox reactions of $Li^+$ ions, where Li ions are intercalated in NLSG and $PF_6^-$ anions simultaneously accumulated at the electrode/electrolyte interface.[23] CV curves at various scan rates can provide qualitative estimation of Li-ion diffusion kinetics by computing the *b* value in the chosen window of scan rates, as shown in Figure S13. Current response is given by the power law relationship as $i = av^b$, where *i* is current, *v* is scan rate, *a* and *b* are constants. By plotting $\log^i$ against $\log^v$, the *b* value can be calculated from the slope, which gives two critical conditions: $b = 0.5$ and $b = 1$. The former indicates a typical faradaic intercalation process controlled by semi-infinite linear diffusion; the latter represents capacitive charge storage free of diffusion control. As shown in Figure S13b, the anodic peak current at 2.3 V

gives a *b* value of 0.87 in the scan rate range of 1-10 mV $s^{-1}$, while the *b* value of cathodic peaks at 2.5 V is 0.88, suggesting a fast kinetics dominated by pseudocapacitive process.[7]

The electrochemical impedance spectroscopy (EIS) was carried out to better understand the reaction kinetics and electrical conductivities of NLSG//PC Li-ion capacitor, as shown in Figure S14. The high-frequency semicircle is assigned to the charge-transfer resistance and the double-layer capacitance of electrode-electrolyte interface, reflecting two processes: anions that adsorb/desorb onto/from the surface of positive electrodes, and Li ions that pass through from the electrolyte to the surface of negative electrodes. The line corresponds to the Li ion diffusion process, indicating that Li ions intercalate/de-intercalate in the bulk of the negative electrode. After 10 cycles, the semicircle becomes more obvious, indicating that the charge-transfer resistance increases with cycling. In addition, both the real and imaginary parts of impedance for the 10th cycle are larger than that of the first cycle, which is attributed to the increased diffusion and migration pathways of electrolyte ions during the charge/discharge process.[7]

The specific capacities of the as-assembled HLIC were characterized by galvanostatic charge/discharge tests in a wide voltage window of 0.01–4.0 V with different current densities. The charge and discharge curves of the NLSG//PC hybrid Li-ion capacitors at different current densities show little deviation from the linear slope (Figure 4b), indicating that the devices exhibit charge/discharge performance of a combination of battery and supercapacitor. For NLSG//PC hybrid Li-ion capacitor device, the specific capacitance values (based on total mass of electrode materials) are 85.2, 78.2, 72.5, 63.4, 54.2, 45.1, and 33.2 F $g^{-1}$ at the current densities of 0.1, 0.2, 0.5, 1, 2, 5, and 10 A $g^{-1}$, respectively. Furthermore, the NLSG//PC hybrid Li-ion capacitor showed 87.5% capacitance retention after 5000 cycles when tested at a current density of 1 A $g^{-1}$ and a coulombic efficiency of nearly 100% (Figure 4c). Beyond that, our

NLSG and PC electrodes can also be appied on hybrid Na-ion capacitors, more details can be found in Supporting information (Figure S9-S11).

Figure 4d present the Ragone plots of NLSG//PC hybird Li-ion capacitors compared to some hybrid devices reported in the literature.[4a, 8a, 23-24] The energy density and power density were calculated based on the total mass of active materials in both electrodes. It is noted that the NLSG//PC hybrid Li-ion capacitor can achieve an energy density of 186 W h $kg^{-1}$ at a power density of 200 W $kg^{-1}$. Even at a high power density of 20 kW $kg^{-1}$, our device can still deliver an energy density of 76 W h $kg^{-1}$. The high energy density and high power capability of the NLSG//PC hybrid LI-ion capacitors match the best performance of recently reported HLICs. The summary of the performance of reported hybrid Li-ion capacitors were shown in Table S1.

The assembled NLSG//PC hybird Li-ion capacitors exhibit outstanding electrochemical performance including high energy density, high power density, and long cycle life. These characteristics can be attributed to the following factors: (1) Nitrogen doping and laser scribing process expand the carbon interlayer spacing to 0.38 nm, which facilitates diffusion of $Li^+$ ions in the cathode. (2) The rich oxygen atom, pyridinic N and pyrrolic N functionalities create a large number of active sites at the surface to enhance the surface capacity contribution. Furthermore, the graphitic N can improve the conductivity of the electrode. (3) The 3D interconnected conductive network builds up an expressway for fast electron transfer, and the large surface area with abundant micropores can greatly increase the electrolyte/electrode interface, resulting in large pseudocapacitance contribution and facile electrolyte penetration into the active material.

## EXPERIMENTAL SECTION

**Sample Preparation**

**Preparation of NLSG:** 12.8 wt% Polyamic acid (PAA) solution, dissolved in N-methylpyrrolidone, was purchased from the Sigma-Aldrich company. 15 wt % weight percentages of urea (relative to PAA) were added to the PAA solution and mixed under magnetic stirring for 24 hours to form a uniform precursor solution. To form the battery electrodes directly, a urea-containing PAA solution was dispensed onto the Cu foil followed by scraping using a manual scraper. Subsequently, the film was dried upon evaporation of the NMP solvent in a vacuum oven at 80 ℃ for two hours, resulting in a solid PAA/urea film attached to Cu foil. The PAA/urea film was then dehydrated at a temperature of 150 ℃ at a pressure of ~0.4 MPa for 30 minutes to complete the formation of the urea-containing PI film. Finally, the films were exposed to $CO_2$ laser irradiation in $N_2$ gas ambient.

The laser was generated with the Universal X-660 laser cutter platform (Professional laser system PLS6.75, laser peak power 75 W). The wavelength of the laser was 10.6 μm, and the pulse duration was approximately 14 μs. The pulses per inch (PPI) were set to 1,000, and the image quality level was set to seven for all experiments. The z-distance between the laser and the sample was optimized to 3 mm. Power of laser was set to be 5.0 W. Corel Draw software was employed to design the patterns on PI films. The beam size was roughly 100 μm.

**Preparation of PC:** First, 37.2 g EDTA disodium salt dihydrate was mixed with 8 g NaOH in 200 mL deionized water with stirring at 80 ℃ for 24 hours, and then dried at 80 ℃ to form EDTA tetrasodium salt powders. PC was obtained by pyrolysis of EDTA tetrasodium salt in nickel crucible at 700 ℃ for 1 hour with a ramping rate of 2 ℃ $min^{-1}$ in argon atmosphere

**Material Characterization**

For the powder X-ray diffraction (XRD) tests, the samples were scanned from 10° to 80° at a scan rate of 5° per second by a Bruker diffractometer (D8 Advance) with Cu Kα radiation. Raman spectra were recorded using a Hariba LabRAM HR spectrometer with a He-Ne laser with a wavelength of 633 nm at 50× objective lens. XPS was performed with a Kratos AXIS Ultra DVD (Kratos Analytical Ltd) at a base pressure of $1 \times 10^{-9}$ Torr with a monochromatic Al Kα X-ray source operating at 150 W. The morphology of the samples was characterized by scanning electron microscope (SEM) with FEI Nova Nano 630 microscope and High-resolution transmission electron microscope (HRTEM) using FEI Titan operating at 80–300 KV. The surface areas and pore distributions of the samples were measured by the BrunauerEmmett-Teller (BET) method, using ASAP 2420 (Surface area and pore size analyzer, micromeritics) at a bath temperature of -195.85 °C and N2 as the adsorbate gas. The atomic force microscope (AFM, 5500 Agilent Technologies) was used to determine the thickness and size of the samples. The Thermogravimetric analysis (TGA) was carried using a Netzsch TG 209 F1 instrument from 25 to 1000 °C at a heating rate of 10 °C $min^{-1}$ in the $N_2$ atmosphere.

**Electrochemical Measurements**

All the samples were directly used as electrodes without any binders or conducting additives. Half cells using Li or Na foil as both counter and reference electrodes were assembled in R2032-type coin cells in a glove box. Celgard 3501 microporous membranes were used as the separator, and 1 m $LiPF_6$ or $NaPF_6$ in ethylene carbonate and diethyl carbonate (EC/DEC, v/v = 1:1) solution were used as the electrolytes. Cyclic voltammetry was performed on a VMP3 (Biologic, France) electrochemical workstation. Galvanostatic discharge and charge at different current densities were measured with an Arbin BT-2043 battery testing system. The mass

loadings of the NLSG electrodes were in the range of 1.5–2 mg $cm^{-2}$. Pre-lithiated or pre-sodiated NLSG were used as the anode and porous carbon was used as the cathode with an optimized cathode/anode mass ratio of about 3:1. During the pre-lithiation process, the anode was assembled with the Li foil as the half-cell in the same electrolyte and charged/discharged for 5 cycles. Then, the battery was disconnected and disassembled at 0.05V (discharge state), and the anode material was washed with DEC and taken to the assembly of coin cell-type hybrid device. The pre-sodiation process was done in similar fashion, but using Na foil and $NaPF_6$ as electrolyte.

The energy density (E) and power density (P) were calculated from the galvanostatic charge/discharge process curve by the equation:

$$E = \int_{t2}^{t1} IV\,dt$$

Where E (Wh $kg^{-1}$) is energy density, I is the constant current density (A $g^{-1}$), V is the voltage, and t1, t2 is the start time and end time in the discharge process, respectively.

$$P = \frac{E}{\Delta t}$$

Where P is power density (W $kg^{-1}$), and t is discharge time (s). The mass used in the calculations included both cathode and anode active materials.

## ASSOCIATED CONTENT

**Supporting Information**

## AUTHOR INFORMATION

**Corresponding Author**

*E-mail (Husam N. Alshareef): husam.alshareef@kaust.edu.sa;

**Notes**

The authors declare no competing financial interest.

## ACKNOWLEDGEMENTS

The research reported in this publication was supported by King Abdullah University of Science and Technology (KAUST) under the KAUST-King Saud University Battery Initiative (KAUST Grant # REP/1/3804-01). The authors thank the Core Laboratory Staff at KAUST for their support. M.A.D. and Z.A. greatly acknowledge Deanship of Scientific Research at King Saud University for funding research grant no RG#1440-115.

## Reference

[1] a) I. H. Son, J. H. Park, S. Kwon, S. Park, M. H. Rümmeli, A. Bachmatiuk, H. J. Song, J. Ku, J. W. Choi, J.-m. Choi, *Nat. Commun.* **2015**, 6, 7393; b) J. Janek, W. G. Zeier, *Energy* **2016**, 500, 300.

[2] a) H. Li, M. Yu, F. Wang, P. Liu, Y. Liang, J. Xiao, C. Wang, Y. Tong, G. Yang, *Nat. Commun.* **2013**, 4, 1894; b) H. Ji, X. Zhao, Z. Qiao, J. Jung, Y. Zhu, Y. Lu, L. L. Zhang, A. H. MacDonald, R. S. Ruoff, *Nat. Commun.* **2014**, 5, 3317.

[3] J. Ding, W. Hu, E. Paek, D. Mitlin, *Chem. Rev.* **2018**, 118, 6457.

[4] a) Z. Le, F. Liu, P. Nie, X. Li, X. Liu, Z. Bian, G. Chen, H. B. Wu, Y. Lu, *ACS Nano* **2017**, 11, 2952; b) H. Wang, C. Zhu, D. Chao, Q. Yan, H. J. Fan, *Adv. Mater.* **2017**, 29, 1702093.

[5] a) R. Kiruthiga, C. Nithya, R. Karvembu, *Electrochim. Acta* **2017**, 256, 221; b) A. K. Solarajan, V. Murugadoss, S. Angaiah, *J. Appl. Polym. Sci.* **2017**, 134, 45177; c) S. Zhang, C. Li, X. Zhang, X. Sun, K. Wang, Y. Ma, *ACS Appl. Mater. Interfaces* **2017**, 9, 17136.

[6] a) H. Li, L. Peng, Y. Zhu, X. Zhang, G. Yu, *Nano Lett.* **2016**, 16, 5938; b) W. Cao, J. Zheng, *J. Power Sources* **2012**, 213, 180.

[7] a) J. Ding, H. Wang, Z. Li, K. Cui, D. Karpuzov, X. Tan, A. Kohandehghan, D. Mitlin, *Energy Environ. Sci.* **2015**, 8, 941; b) S. Sivakkumar, J. Nerkar, A. Pandolfo, *Electrochim. Acta* **2010**, 55, 3330.

[8] a) S. Deng, J. Li, S. Sun, H. Wang, J. Liu, H. Yan, *Electrochim. Acta* **2014**, 146, 37; b) P. Nayak, N. Kurra, C. Xia, H. N. Alshareef, *Adv. Electron. Mater.* **2016**, 2, 1600185; c) J. Lin, Z. Peng, Y. Liu, F. Ruiz-Zepeda, R. Ye, E. L. Samuel, M. J. Yacaman, B. I. Yakobson, J. M. Tour, *Nat. Commun.* **2014**, 5, 5714.

[9] F. Zhang, E. Alhajji, Y. Lei, N. Kurra, H. N. Alshareef, *Adv. Energy Mater.* **2018**, 8, 1800353.

[10] N. Kurra, Q. Jiang, P. Nayak, H. N. Alshareef, *Nano Today* **2019**.

[11] Y. Wen, K. He, Y. Zhu, F. Han, Y. Xu, I. Matsuda, Y. Ishii, J. Cumings, C. Wang, *Nat. Commun.* **2014**, 5, 4033.

[12] Z. Li, C. Lu, Z. Xia, Y. Zhou, Z. Luo, *Carbon* **2007**, 45, 1686.

[13] K. N. Kudin, B. Ozbas, H. C. Schniepp, R. K. Prud'Homme, I. A. Aksay, R. Car, *Nano Lett.* **2008**, 8, 36.

[14] A. C. Ferrari, D. M. Basko, *Nature nanotechnology* **2013**, 8, 235.

[15] M. Mao, C. Cui, M. Wu, M. Zhang, T. Gao, X. Fan, J. Chen, T. Wang, J. Ma, C. Wang, *Nano Energy* **2018**, 45, 346.

[16] a) L. Fu, K. Tang, K. Song, P. A. van Aken, Y. Yu, J. Maier, *Nanoscale* **2014**, 6, 1384; b) Q. Pang, J. Tang, H. Huang, X. Liang, C. Hart, K. C. Tam, L. F. Nazar, *Adv. Mater.* **2015**, 27, 6021.
[17] Z. Li, Z. Xu, X. Tan, H. Wang, C. M. Holt, T. Stephenson, B. C. Olsen, D. Mitlin, *Energy Environ. Sci.* **2013**, 6, 871.
[18] P. Kichambare, J. Kumar, S. Rodrigues, B. Kumar, *J. Power Sources* **2011**, 196, 3310.
[19] L.-F. Cui, Y. Yang, C.-M. Hsu, Y. Cui, *Nano Lett.* **2009**, 9, 3370.
[20] M. Endo, C. Kim, K. Nishimura, T. Fujino, K. Miyashita, *Carbon* **2000**, 38, 183.
[21] H. Wang, Y. Zhang, H. Ang, Y. Zhang, H. T. Tan, Y. Zhang, Y. Guo, J. B. Franklin, X. L. Wu, M. Srinivasan, *Adv. Funct. Mater.* **2016**, 26, 3082.
[22] S. Sivakkumar, A. Pandolfo, *Electrochim. Acta* **2012**, 65, 280.
[23] N. Kurra, M. Alhabeb, K. Maleski, C.-H. Wang, H. N. Alshareef, Y. Gogotsi, *ACS Energy Letters* **2018**, 3, 2094.
[24] a) Z. Chen, Y. Yuan, H. Zhou, X. Wang, Z. Gan, F. Wang, Y. Lu, *Adv. Mater.* **2014**, 26, 339; b) T. Zhang, F. Zhang, L. Zhang, Y. Lu, Y. Zhang, X. Yang, Y. Ma, Y. Huang, *Carbon* **2015**, 92, 106; c) V. Khomenko, E. Raymundo-Piñero, F. Béguin, *J. Power Sources* **2008**, 177, 643; d) R. Yi, S. Chen, J. Song, M. L. Gordin, A. Manivannan, D. Wang, *Adv. Funct. Mater.* **2014**, 24, 7433; e) S. Dong, L. Shen, H. Li, G. Pang, H. Dou, X. Zhang, *Adv. Funct. Mater.* **2016**, 26, 3703; f) E. Lim, C. Jo, M. S. Kim, M. H. Kim, J. Chun, H. Kim, J. Park, K. C. Roh, K. Kang, S. Yoon, *Adv. Funct. Mater.* **2016**, 26, 3711.

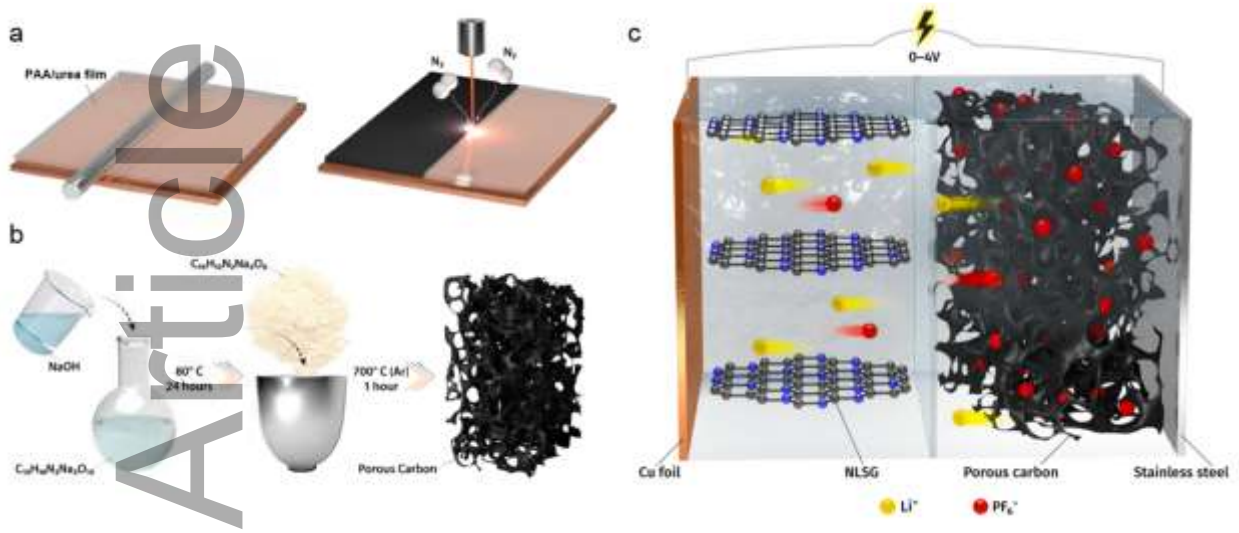


**Figure 1**. Schematic illustrating the process used to fabricate (a) nitrogen-doped 3D graphene (NLSG) anodes and (b) EDTA tetrasodium salt-derived porous carbon cathodes (PC). (c) Schematic of the assembled all-carbon hybird mobile ion capacitor device.

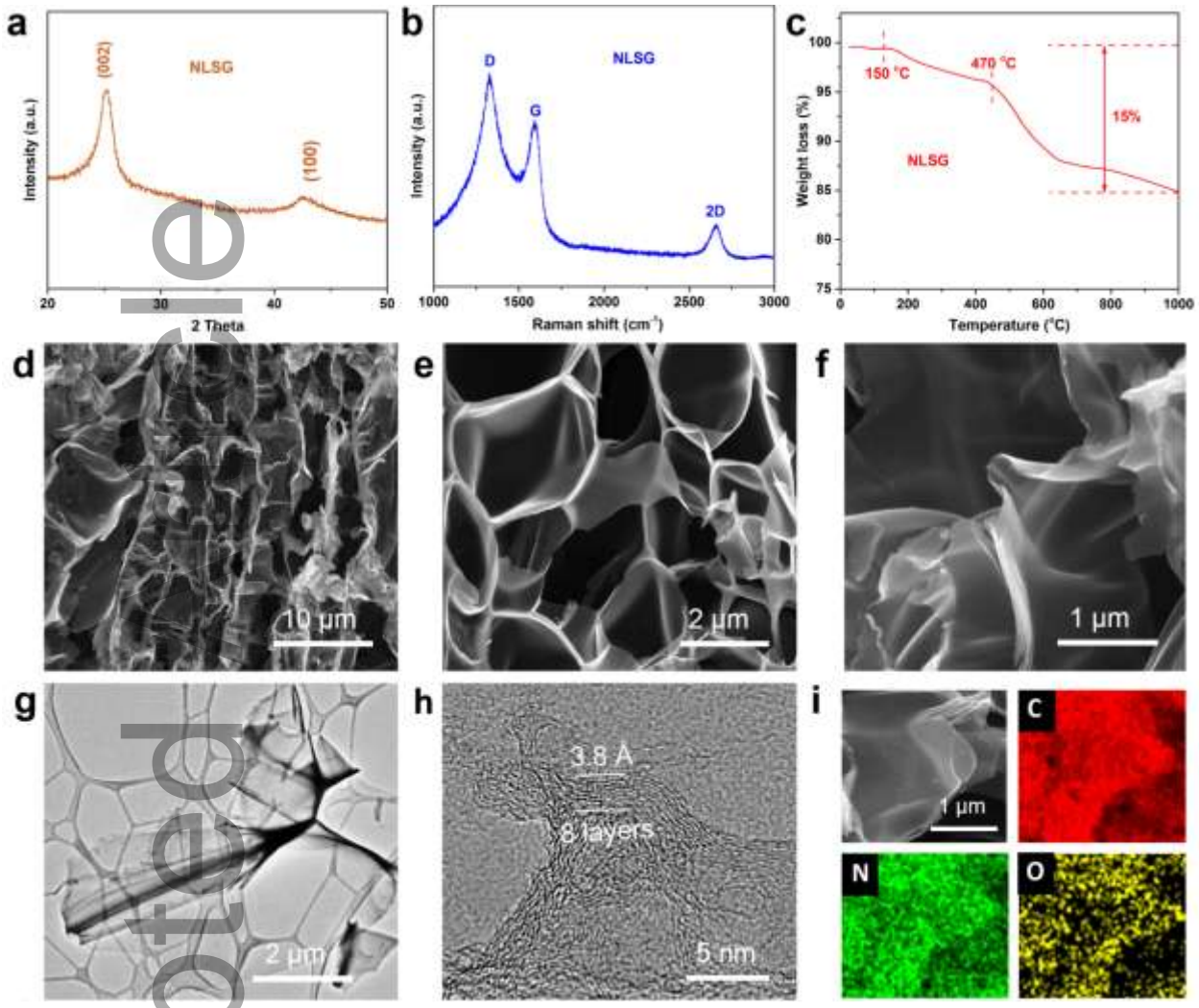


**Figure 2**. (a) XRD patterns of NLSG; (b) Raman spectra of NLSG; (c) TGA curve of NLSG; (d-f) SEM images depicting the morphology of NLSG with different magnification; (g) TEM image of one NLSG nanosheet; (h) HRTEM image of NLSG nanosheet with interlayer spacing; (i) EDS mapping of NLSG with elemental C, N and O.

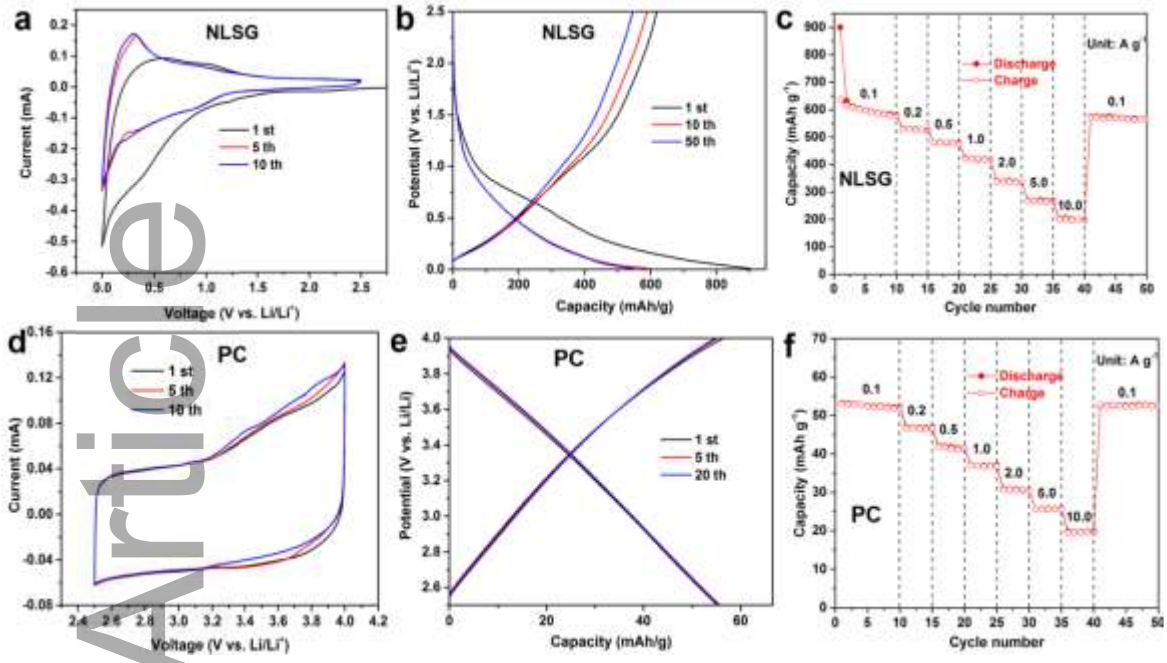


**Figure 3**. Performances of Li half-cell: CV curves of (a) NLSG, (d) PC at 0.1 mV $s^{-1}$; Galvanostatic charge/discharge profiles of (b) NLSG (e) PC for the 1st, 10th and 50th cycles at 0.1 A $g^{-1}$; Rate performance of (c) NLSG, (f) PC at different current densities.

,

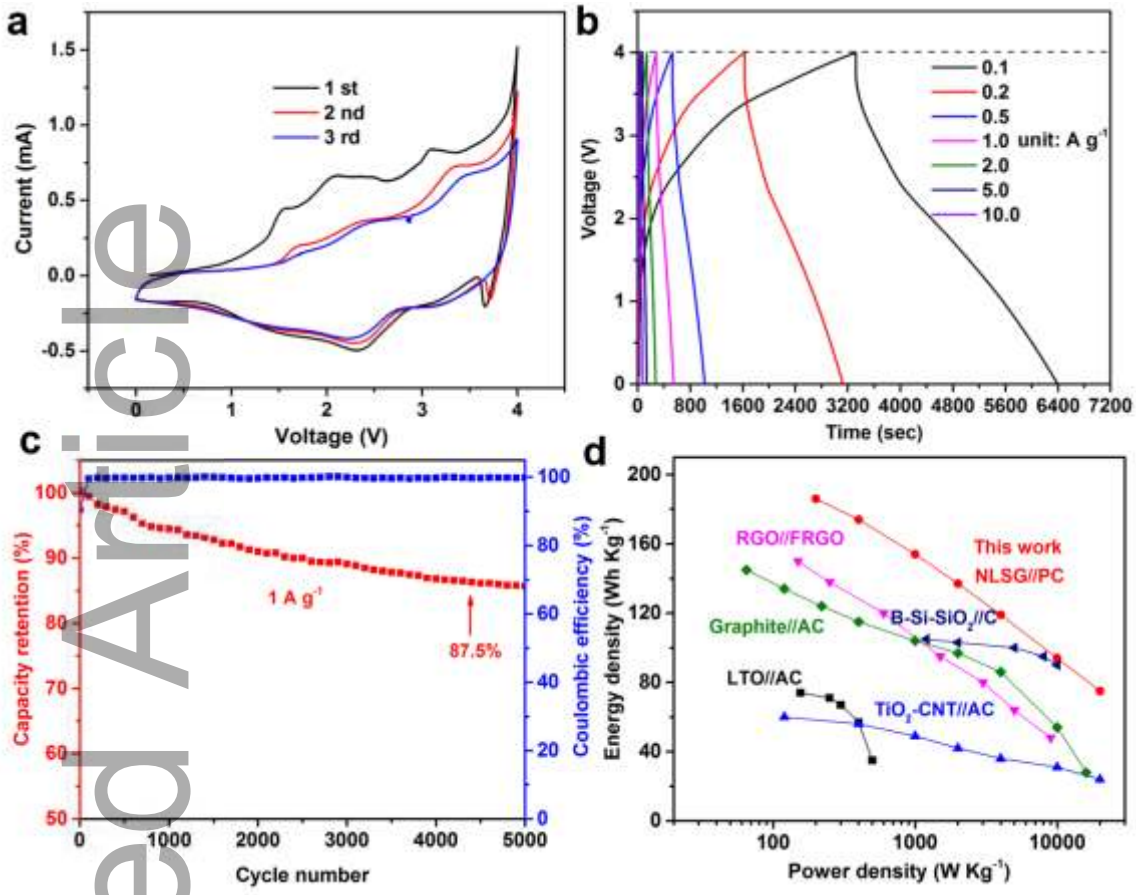


**Figure 4**. (a) CV curves of the NLSG//PC hybird Li-ion capacitor at 1 mV $s^{-1}$. (b) Charge–discharge curves of the NLSG//PC hybird Li-ion capacitor at different current density. (c) Cycle performance of the NLSG//PC hybird Li-ion capacitor between 0.01 and 4.0 V at a current density of 1 A $g^{-1}$. (d) Ragone plots comparing the present NLSG//PC hybrid Li-ion capacitor with previously reported HLICs (including the total weight of two electrodes).

# TOC



**All-Carbon Hybrid Mobile Ion Capacitors Enabled by 3D Laser Scribed Graphene:** Laser scribed nitrogen-doped 3D graphene (NLSG) is demonstrated as binder-free, conductive, and additive-free anode for hybrid Li-ion capacitors (HLIC). The hybrid capacitors are assembled by combining 3D graphene anodes with porous carbon (PC) cathodes obtained by pyrolysis of Ethylenediaminetetraacetic (EDTA tetrasodium salt. The NLSG//PC hybrid Li-ion capacitors show an energy density (including the total weight of two electrodes) of 186 Wh kg−1 at 200 W $kg^{-1}$.

**Keyword:** LSG, laser scribed graphene, mobile ion capacitors

Fan Zhang[a], Wenli Zhang[a], Jing Guo[a], Yongjiu Lei[a], Mushtaq A. Dar[b], Zeyad Almutairi [c,d], Husam N. Alshareef [a,*]

All-Carbon Hybrid Mobile Ion Capacitors Enabled by 3D Laser Scribed Graphene